



OPEN Field test and numerical research on explosion crater in calcareous sand

Changchun Li^{1,2,4}, Yumin Chen^{2,3}✉, Yingkang Yao¹, Yonggang Gou², Qiongtong Wang², Junwei Guo², Xiao Xie² & Xiangyu Wang^{4,5}✉

The explosion in foundation poses a significant threat to people and buildings. Currently, a unified empirical prediction formula for crater in calcareous foundation has not been established. In this paper, analyzed the types and sizes of explosion crater with different scaled burial depths through field tests and numerical simulation. In field tests, revealed the influence of scaled burial depth on the type and size of explosion crater and obtained the critical scaled burial depth for three different types of explosion craters, namely ejecta-type crater, collapse-type crater and covert explosion. Through the Smooth Particle Hydrodynamic-Finite Element Method (SPH-FEM) coupling algorithm, studied the movement trajectory of sand particles around the explosive at the moment of explosion in detail. Based on the field tests and numerical simulation results, it was found that calcareous sand has a smaller specific gravity due to its own characteristics, and the size of the explosion crater is larger than that of quartz sand at the same scaled burial depth. Obtained an empirical formula for crater in calcareous sand. Which can quickly predict the size of explosion crater and provide calculation basis for explosion resistant design in calcareous sand foundations.

Keywords Field test, SPH-FEM, Calcareous sand, Scaled burial depth, Crater

Calcareous sand is widely distributed in subtropical and tropical continents and coastal cities, such as the South China Sea, the Australian Great Barrier Reef and other coral islands¹. Calcareous sand is formed by long-term geological weathering of organic matter and coral debris in the ocean, and its content is more than 90% calcium carbonate². Due to its special formation mechanism, it has the characteristics of irregular shape, large porosity and easy crushing, and has significantly different physical and mechanical properties from quartz sand^{3,4}. Calcareous sand is widely used as backfill material in human living areas on islands⁵. The explosion of underground pipelines and the use of controlled explosion to reinforce foundations inevitably involve explosions in sand foundations. Therefore, it is of great significance to carry out explosion research in calcareous sand foundations.

The explosion mechanism of the sand is relatively complex, as it involves the interaction of material nonlinearity, geometric nonlinearity and multiphase media⁶. The explosion crater is a direct response to the explosion loading in the sand⁷. The energy generated by the explosion and the pressure of the sand above the explosive play a decisive role in the type and size of the explosion crater⁸.

Methods for the mechanism of explosion crater can be classified into three main categories: Firstly, theoretical analysis enables the study of explosions in sand⁹. Based on the theoretical analysis of the similarity principle, some calculation parameters can be reasonably assumed and simplified to derive the dimensionless relationship between the diameter of the explosion crater, the energy of the explosive and the burial depth¹⁰. Therefore, the theoretical analysis method has the advantages of simple calculation form and broad application range^{11–13}.

Secondly, field test remains an effective method for researching the explosions in sand¹⁴. Researchers from the University of Argentina and Hohai University conducted field tests in clay and Yangtze River sand respectively, and found that the scaled burial depth of explosive plays a decisive role in the shape and size of the explosion crater^{15,16}. When the explosive is buried shallowly, the energy generated by the explosion is mainly due to the splashing of the sand above the explosive¹⁷. As the burial depth of the explosive increases, the suppression effect of the sand above the explosive on the energy generated by the explosion gradually increases under the action

¹State Key Laboratory of Precision Blasting, Jiangnan University, Wuhan 430056, China. ²College of Civil and Transportation Engineering, Hohai University, Nanjing 210024, China. ³School of Civil Engineering, Suzhou University of Science and Technology, Suzhou 215011, Jiangsu, China. ⁴School of Design and Built Environment, Curtin University, Perth, WA 6102, Australia. ⁵School of Civil Engineering and Architecture, East China Jiao Tong University, Nanchang 330013, China. ✉email: ymch@hhu.edu.cn; Xiangyu.Wang@curtin.edu.au

of gravity, thus changing the type of explosion crater. And the empirical prediction formula for explosion crater was derived based on field test results.

Thirdly, numerical simulation method can better to explain the explosion problems in sand with the rapid development of computer software and hardware technology¹⁸. The Arbitrary Lagrangian-Eulerian (ALE) method uses the characteristics of the Lagrangian method to deal with structural boundary motion, absorbs the advantages of the Euler method for meshing, and can handle the large deformation problem of explosions in sand quickly¹⁹. However, ALE method has the disadvantage of non-smooth boundaries, and the element incompatibility leads to non-physical penetration of Euler matter.

The SPH method can effectively improve the calculation accuracy, but the speed of calculation is very slow. SPH-FEM is a method that couples smooth particle hydrodynamic and finite element method²⁰. The SPH particles were placed in area of large deformation and finite elements were set in areas of small deformation. Which can not only accurately represent the disaster mechanism but also enhances computational efficiency. As a result, the SPH-FEM method gained widespread application in geotechnical engineering²¹.

The SPH-FEM method is used to simulated the mobility of soil particles during slope instability^{22,23} and migration of soil particles during soil densification under strong compaction²⁴. At the same time, the SPH-FEM method can also effectively simulate the local high stress area formed by the impact pile in the soil and analyze the yield and stress redistribution phenomenon of the soil around the pile²⁵. Besides, the SPH-FEM method can simulate the deformation the underground structure under dynamic loads, and track the location information and motion of soils at any moment^{26–28}.

However, existing research on explosions in sand primarily focuses on rock, clay, and quartz sand, with relatively little research conducted on calcareous sand foundations^{29–31}. With the rise in production activities involving explosions in calcareous sand foundations, and given that its physical and mechanical properties differ significantly from quartz sand, there is an urgent need for research in this area. The issue of explosions in sand can be better understood through a combination of field tests and numerical analysis.

Considering the ability of SPH-FEM method to effectively handle large deformations and effectively describe the motion trajectory of sand particles under explosion loads. In this study, we investigated the type and size of craters in calcareous sand foundations through field tests and SPH-FEM method. Furthermore, based on the results from both field tests and numerical analysis, an empirical prediction formula for craters in calcareous sand foundations was derived, providing a theoretical reference for explosion-resistant design and foundation reinforcement.

Method

Theory

The scaled burial depth

High-energy chemical explosives generate high-temperature, high-pressure gases, which exert a strong radial compression on the surrounding sand medium, forming a compaction zone³². The TNT equivalent and the burial depth of the explosive have a significant impact on the type and size of the explosion crater³³. To assess the destructive effects of different types of explosive sources under the same conditions, the concept of scaled burial depth is typically introduced to evaluate the explosion damage effects across various explosions under consistent conditions³⁴, as shown in Eq. (1):

$$z = \frac{d}{(W_{TNT})^{1/3}} \quad (1)$$

where, z is the scaled burial depth, d is the burial depth, W_{TNT} is the explosive's TNT equivalent.

The buried depth of the explosive determines the type and size of the explosion crater³⁵. When the buried depth of the explosive is small, the detonation gas generated after the explosion quickly squeezes the sand around the explosive, and the explosion compression effect and peeling effect causes the sand around the explosive to gain an upward initial velocity and cause a throwing phenomenon, forming an ejecta-type crater, as shown in Fig. 1³⁶. As the burial depth of the explosive increases, the inhibitory effect of the sand covering the explosive on the throwing of the explosion gradually increases. The detonation gas only causes the local sand around the explosive to form a small cavity, and the cavity collapses under the weight of the upper sand, eventually forming a collapsed-crater, as shown in Fig. 2³⁷. As the burial depth of explosives continues to increase, the energy generated by the explosion can only provide vibrations to the foundation, there is no obvious change in the surface, and a camouflet is formed³⁸.

Aspect ratio

On the basis of the scaling law, any linear dimension L of the explosion crater can be indicated as a constant multiplied by the equivalent TNT of the explosive W^a , where a is a coefficient dependent on whether neglected the gravity³⁹. Baker et al. presented a dimensional study with six parameters to model the crater formation phenomenon in underground explosion¹⁰. Obtained the aspect ratio (r_c) functional as shown in Eq. (2), after many analyzes and observations.

$$r_c = \frac{R}{d} = f \left[\frac{W^{7/4}}{\sigma^{1/6} K^{1/8} d} \right] \quad (2)$$

where, W is equivalent TNT of the explosive; d is the depth of the explosive; R is radius of the crater; σ is dimensions of stress, which was related to the sand strength; K is dimensions of a force divided by a cubic length.

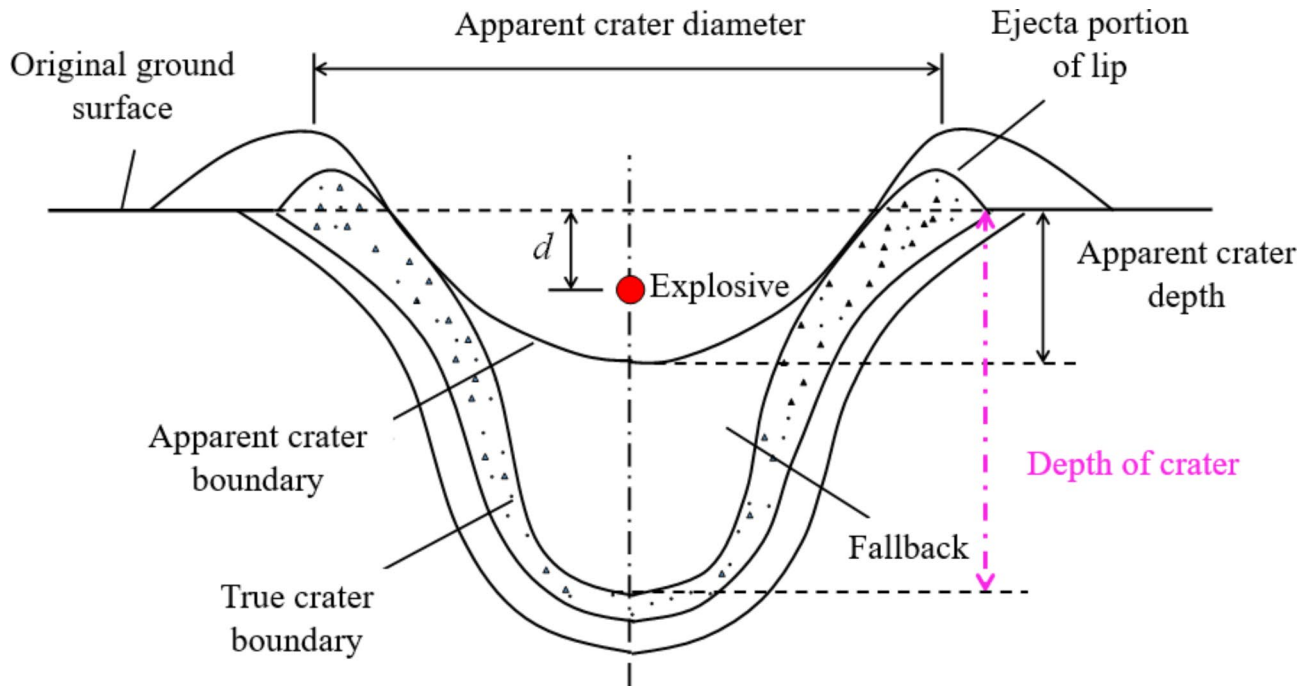


Fig. 1. The ejecta-type crater.

As shown in Eq. (2), the specific weight ρg is measured for K , ρc^2 is measured for σ , where c is the explosion velocity in the sand. If this empirical formula for different density of sand is plotted in a r_c versus $\frac{W^{2/3}}{\rho^{2/3} c^3 \rho^8 d}$ graph, it can be clearly described that there is a small change in the results.

Field test

Calcareous sand

The sand used in the field test is calcareous sand sourced from the South China Sea, formed through long-term geological and weathering processes of coral in the ocean⁴⁰. The physical picture and electron microscope scanning picture of the calcareous sand are shown in Fig. 3. As shown in Fig. 3, the calcareous sand particles possess unique physical properties, such as an irregular shape and high porosity. The grain size distribution curve of the calcareous sand is shown in Fig. 4. The mechanical parameters of calcareous sand, obtained according to the Chinese Standard for Geotechnical Testing Method, are presented in Table 1.

Design of field test

Large TNT equivalent explosions in sand release enormous amounts of energy, requiring higher-standard testing equipment and stringent safety measures, which inevitably increase both the cost and duration of testing⁴¹. Small TNT equivalent explosions in sand are often more recommended for testing⁴². In the field test, the explosive used was factory-customized black powder with a TNT equivalent of 5 g, as shown in Fig. 5. In the field tests, the explosive was buried at the test design depth and connected to the fuse, as shown in Fig. 6. To increase the probability of success in field tests and prevent water in the foundation from wetting the fuse, a 4 mm diameter plastic pipe is wrapped around the fuse.

By changing the burial depth of explosives, different scaled burial depth conditions were set. The burial depth range for the placement of the explosives is set at 0.03 ~ 0.37 m respectively, as shown in Table 2. Considering the discreteness in field tests, three sets of parallel tests were set up under the same burial depth conditions.

Numerical simulation

SPH-FEM coupling algorithm

Smooth particle hydrodynamics is a meshless Lagrangian computational method⁴³. Its adaptability can better handle large deformation problems and can handle material interfaces smoothly and continuously⁴⁴. The SPH method discretizes the problem domain through a series of particles, each of which can carry field variables such as density, velocity, stress and displacement⁴⁵. The SPH method uses an integral expression to approximate a certain field function, and discretizes it into a series summation problem, as shown in Eq. (3). Equation (3) is a general SPH approximate equation, and its schematic is shown in Fig. 7. As shown in Fig. 7, h is the support domain radius of the kernel function. This equation can be used to estimate any field variable in continuous space.

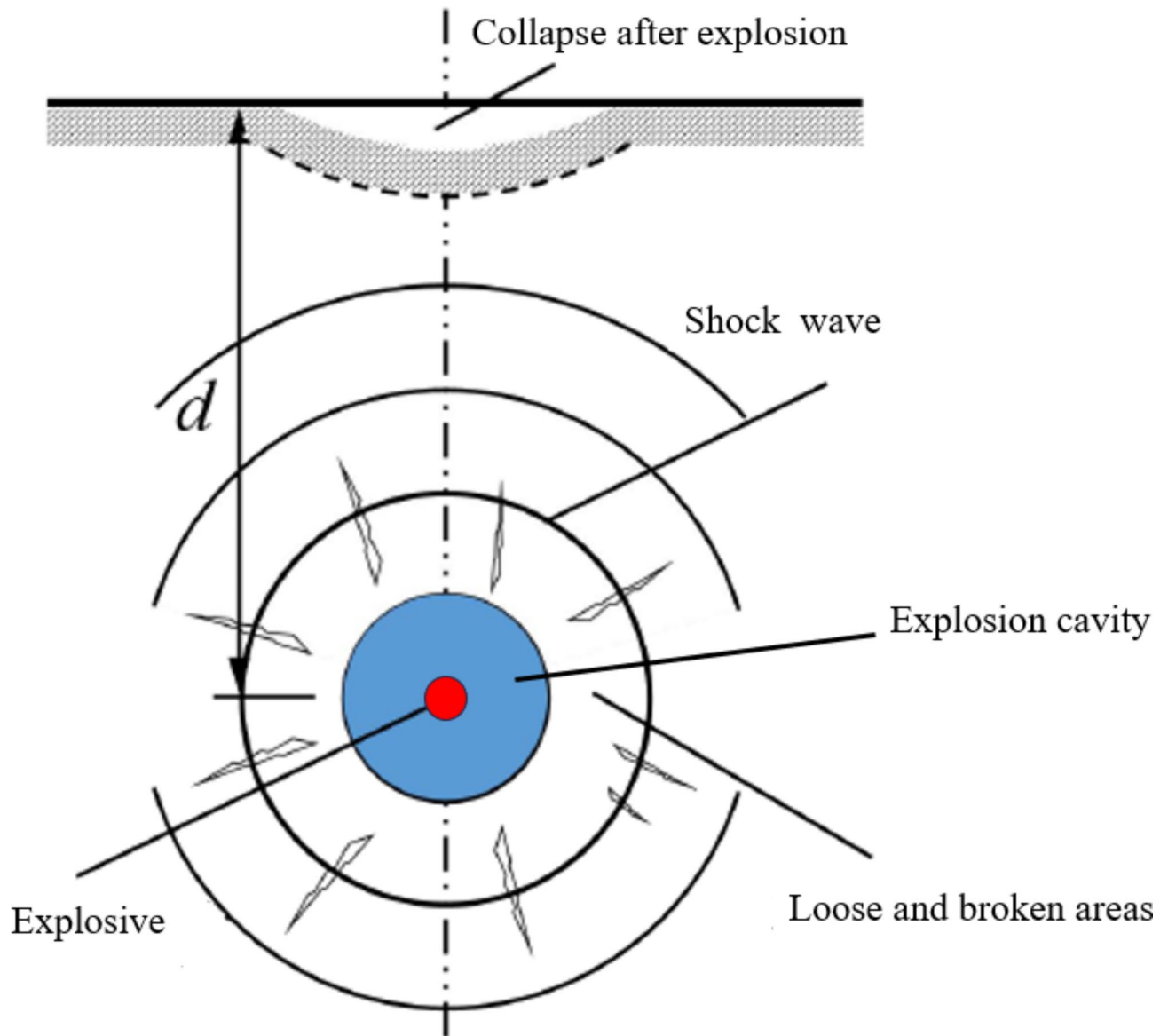


Fig. 2. The collapse-type crater.

$$f(r_i) = \int_{\Omega} f(r)W_{ij}dr \approx \sum_j V_j f_j W_{ij} \quad (3)$$

where, W_{ij} is the kernel function, a dimensionless function; Ω is the support domain of the kernel function; i is the particle studied; j is the particle near i ; r is the distance between particles; V_j is the volume of particle j .

The full SPH particles model will greatly increase the calculation time, and may even cause problems such as limited boundary problems⁴⁶. Therefore, during the modeling process, SPH particles are usually established for the explosive and surrounding sand, and finite elements are used at locations farther away from the explosive. The keyword *CONGTROL_TIED_NODE_TO_SURFACE_OFFSET was used to constrain the mutually fixed coupling between SPH particles and the finite elements, as shown in Fig. 8. Set the SPH particles as the slave surface, set the finite element as the master surface, and constrain the slave nodes to the master surface to realize the transfer of particle speed, stress, mass and other information to the finite elements.

The numerical model

To accurately analyze the characteristics of explosion craters, a 3D finite element model was established based on a 1:1 similarity ratio. The overall size of the numerical model is 0.9 m*0.9 m*0.4 m, among which the range of SPH part is 0.6 m*0.6 m*0.3 m. The dimension of the 1/4 of the numerical model is shown in Fig. 9. The size of element plays a decisive role in calculation accuracy and resource consumption. The trade-off between accuracy and calculation resources is one of the important issues to be solved in numerical analysis. After many trial



Fig. 3. Calcareous sand.

calculations, the size of element in the model was set to 1 cm. The numerical model consists of 223,240 finite elements and 123,068 SPH particles, with 47 SPH particles representing the explosive. By changing the position of the explosive SPH particles, the different burial depth of the explosive in the numerical model is controlled. To simulate the field test as realistically as possible, the top surface of the numerical model is set as a free surface, with normal constraints applied to the sides of the model, and full constraints applied to the bottom.

Calcareous sand model

The key to numerical simulation of explosion problems in sand lies in the reasonable selection of sand models and parameters⁴⁷. By evaluating the constitutive models suitable for describing sand in the LS-DYNA software, the *MAT_005_SOIL_AND_FOAM model, one of the earliest constitutive models that supports the SPH algorithm was selected⁴⁸. This model is simple, with easily obtainable material parameters, and is widely used in addressing explosion problems in calcareous sand foundations.

The loading and unloading stress-strain curves of the model are shown in Fig. 10. Ten sets of data are used to perform multi-segment linear approximation of the compression equation. The equation of state parameters recommended by Wu et al.⁴⁹ and which was suitable for calcareous sand in calculation, as shown in Table 3. The density of calcareous sand is 1370 kg/m³, the shear modulus is 106.3 MPa, the bulk modulus is 587.3 MPa, the shear yield coefficient on the shear plane $a_0 = 73.85 \text{ kPa}^2$, $a_1 = 13.19 \text{ kPa}$, and $a_2 = 0.3$.

The explosive model

The explosive is simulated using the high-energy explosive model and JWL equation in LS-DYNA software³⁷. The JWL equation of the explosive can accurately describe the pressure, volume, and energy characteristics of the explosion during the detonation process, as shown in Eq. (4):

$$P_e = A\left(1 - \frac{\omega}{R_1 V_r}\right)e^{-R_1 V_r} + B\left(1 - \frac{\omega}{R_2 V_r}\right)e^{-R_2 V_r} + \frac{\omega E_0}{V_r} \quad (4)$$

where A , B , R_1 , R_2 and ω are the explosive parameter; P_e is the pressure generated by the explosion; V_r is the relative specific volume; E_0 is the specific internal energy of the explosion products.

The parameters of the explosives used in the paper are shown in Table 4⁵⁰.

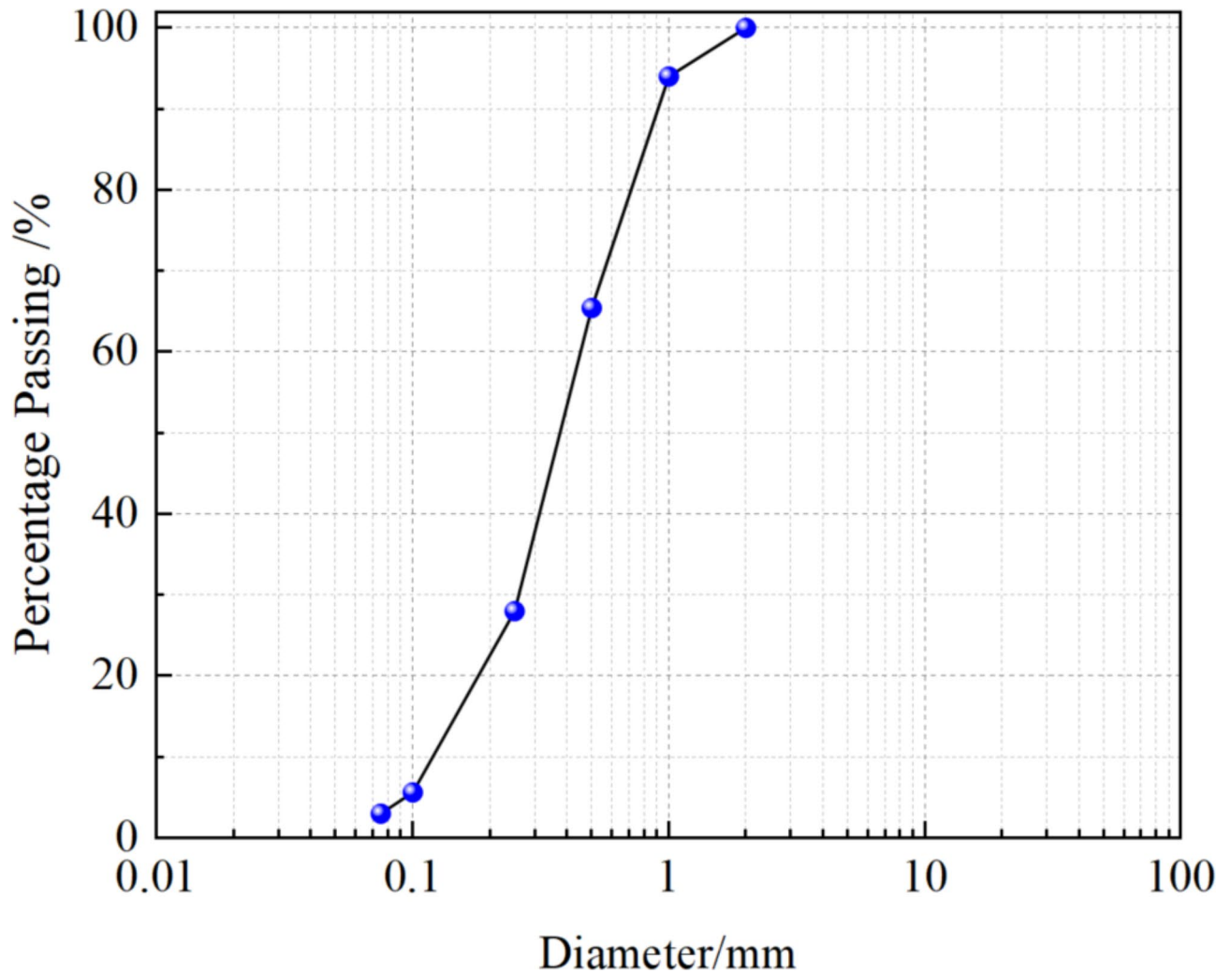


Fig. 4. Grain size distribution curve.

C_u	C_c	w (%)	ρ (g/cm ³)	G_s
3.46	1.25	5.2	1.37	2.72

Table 1. The parameters of the calcareous sand.

Results

Field test results

The formation process of the crater

In the field test, a high-speed camera with a recording frame rate of 60 FPS was used to capture the crater formation process. Taking the scaled burial depth of $0.76 \text{ m/kg}^{1/3}$ as an example, the formation process of crater was shown in Fig. 11. The crater was formed within 300 ms after detonation. The upper calcareous sand on the explosive overcomes the gravity and the bonding forces between sand particles under the explosion loading.

As shown in Fig. 11, within the initial 51 ms, the impact of the explosion induces the calcareous sand above the explosive to move upward, forming a bulge on the surface. Between 51 ~ 136 ms, under the force of the explosion gas, an ejection and splashing phenomenon occurs, forming a pear-like shape. From 136 to 282 ms, the calcareous sand is thrown outward by the explosion impact, and an ejecta-type crater forms under the influence of gravity.

Effect of burial depth on the crater size

When the scaled burial depth of the explosive is small, the explosion mainly causes the calcareous sand particles above the explosive to gain an upward initial velocity and form an ejecta-type crater. When measuring the depth of the ejecta-type crater, it's necessary to remove the sand particles that have fallen back into the top of the crater, as shown in Fig. 12. When measuring the diameter of the crater, test once every 60° , and use the average of the

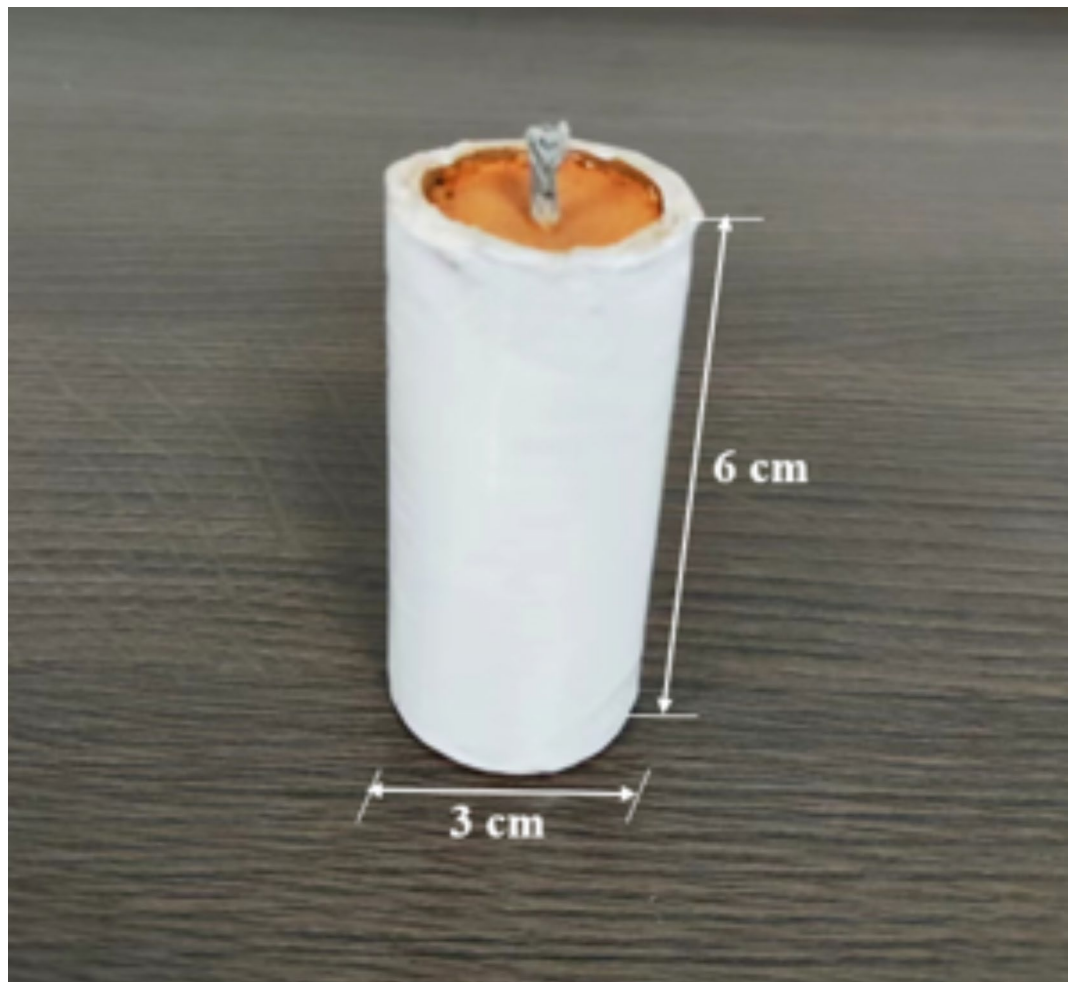


Fig. 5. The explosive.

three measurements as the final measured diameter of the crater, as shown in Fig. 12. The diameter and depth of crater with different scaled burial depths are as shown in Table 4.

It can be seen from Table 5 that when the scaled burial depth is less than $0.53 \text{ m/kg}^{1/3}$, as the burial depth of the explosive increases, the depth and the diameter of the ejecta-type crater gradually increases. When the scaled burial depth is $0.53 \text{ m/kg}^{1/3}$, the diameter of the crater reaches the maximum value, with the maximum diameter of the crater being approximately 0.437 m . When the scaled burial depth is greater than $0.53 \text{ m/kg}^{1/3}$, the diameter of the crater gradually decreases as the scaled burial depth of the explosive increases. At this point, the gravity of the upper sand particles and the friction between particles increase the inhibitory effect on the explosion energy, causing the diameter of the crater to gradually decrease. This result is similar to the quartz sand studied by Jia et al.¹⁶, but there are large differences due to the different parameter of the sand.

The influence of burial depth on the type of crater

When the scaled depth of burial is less than $1.11 \text{ m/kg}^{1/3}$, the energy generated by the explosion dissipates more directly through the free face above the sand, causing the calcareous sand above the explosive to acquire an initial upward velocity and ejection, forming an ejecta-type crater as shown in Fig. 13a. When the scaled burial depth is within 1.11 to $2.05 \text{ m/kg}^{1/3}$, the calcareous sand above the explosive exerts a significant restraining effect on ejection, and the energy generated by the explosion is mainly used for rapidly compressing the surrounding sand. A blast cavity is formed inside the sand, which collapses under the gravity, leading to the observation of clear irregular cracks on the ground surface, resulting in a collapse-type crater as shown in Fig. 13b. When the scaled burial depth exceeds $2.05 \text{ m/kg}^{1/3}$, the gravity of the sand above the explosive predominates. The explosive energy mainly acts on the vibration of the sand foundation, with the energy dissipated through the free face almost negligible. There are almost no visible cracks on the surface at this time, indicating a camouflet is formed in the calcareous sand foundation.

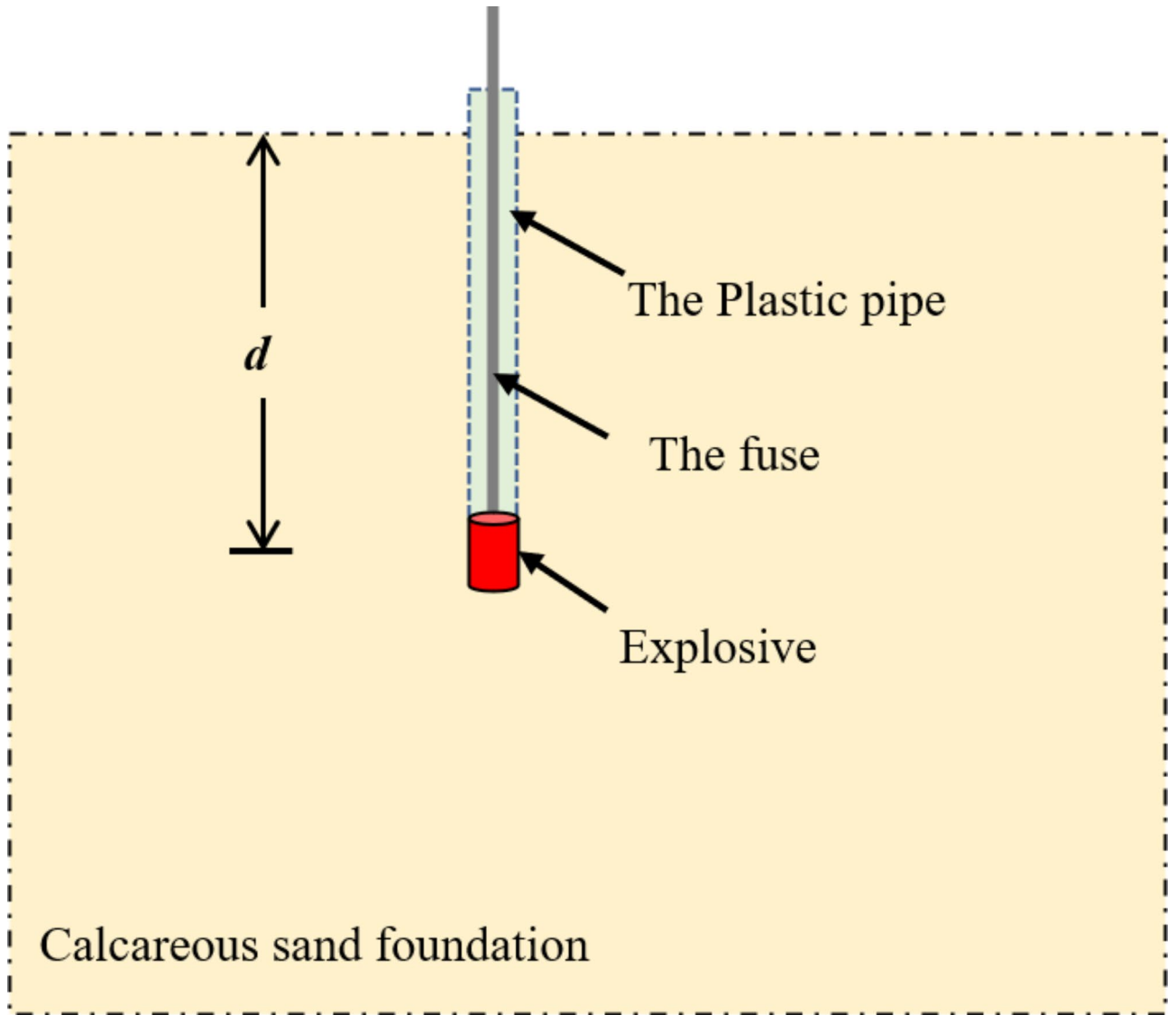


Fig. 6. Experimental diagram.

Test	Depth (m)	The scaled depth (m/kg ^{1/3})	Test	Depth (m)	The scaled depth (m/kg ^{1/3})
BE1	0.03	0.18	BE8	0.17	0.99
BE2	0.05	0.29	BE9	0.19	1.11
BE3	0.07	0.41	BE10	0.21	1.23
BE4	0.09	0.53	BE11	0.23	1.35
BE5	0.11	0.64	BE12	0.33	1.93
BE6	0.13	0.76	BE13	0.35	2.05
BE7	0.15	0.88	BE14	0.37	2.16

Table 2. The design condition of the field test.

Numerical simulation results

Verification of the model

Figure 14 shows the formation process of an ejecta-type crater when the burial depth of explosive is 0.29 m/kg^{1/3}. The formation process of an ejecta-type crater lasts about 300 milliseconds. After the detonation of the explosive, the sand above the explosive is violently thrown due to the expansion of the explosion gases, while the sand at the bottom and around the explosive undergoes substantial plastic deformation due to the explosion shock compression. This ultimately results in the expansion of the crater in both depth and lateral directions. By

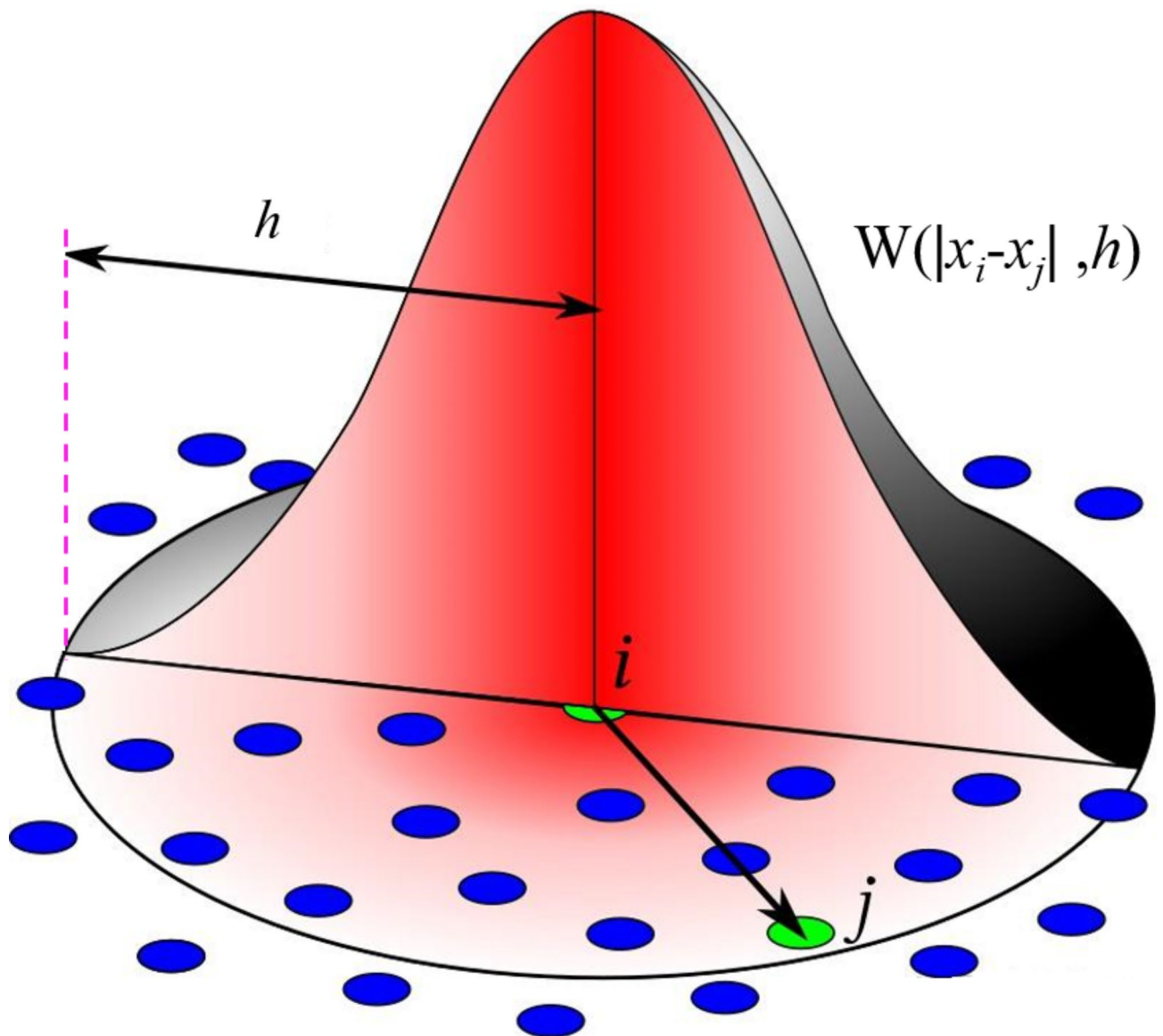


Fig. 7. The schematic of kernel function.

setting sand SPH particles around the explosive, normal calculations can be ensured even under large explosion deformations, the movement of the sand near the explosive can be intuitively described, and a smooth and clear boundary of the ejecta-type crater can be formed. The movement of sand particles observed in Fig. 14 is basically consistent with that captured by high-speed camera in the field test.

When the scaled buried depth of explosive is $0.29 \text{ m/kg}^{1/3}$, the diameter and depth of the ejecta-type crater is as shown in Fig. 15. The diameter and depth of the crater measured were 0.36 m and 0.13 m respectively. The data obtained from the tests are basically consistent with those obtained from field test. It can be considered that the SPH-FEM coupling algorithm can better describe the ejecta-type crater in calcareous sand foundation.

Analysis of crater flow field

When the scaled burial depth of the explosive is $0.41 \text{ m/kg}^{1/3}$, the velocity and displacement vector diagram of the SPH sand particles around the explosive at $t = 50 \text{ ms}$ is shown in Fig. 16. It can be seen from Fig. 16 that after the explosive is detonated, part of the sand around the explosive is radially thrown into the air under the action of the explosion, while the sand on the sides and bottom of the explosive is compressed and compacted approximately along the radial-direction of the sphere at a relatively small speed.

Analysis of different equivalents

Field tests are often constrained by factors such as technical challenges, cost, risk, and limited repeatability. Proven numerical simulations can effectively complement field tests. To investigate the impact of different TNT equivalents on crater size, explosives with TNT equivalents of 5 g, 10 g, and 20 g were used, and the burial depths

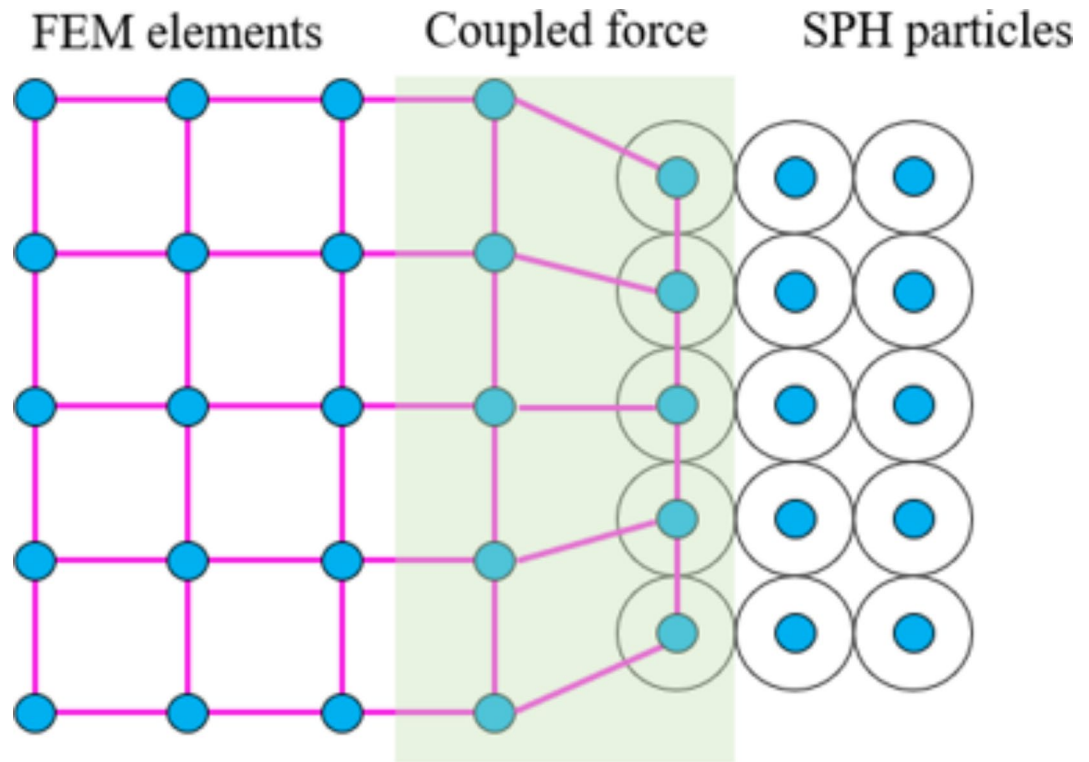


Fig. 8. The SPH-FEM coupling algorithm.

were set according to Table 2. The diameter of the crater under different TNT equivalents is shown in Fig. 17. It can be seen from Fig. 17 that when the TNT equivalent of the explosives is the same, the diameter of the crater first increases and then decreases as the burial depth of the explosive increases. At the same burial depth, the diameter of the crater gradually increases with the increase of the TNT equivalent of the explosive.

As the TNT equivalent and burial depth of the explosive change, the type and size of the crater will show significant variations. Based on the results of field tests and numerical simulations, a comprehensive analysis of the crater diameters at different scaled burial depths has been conducted. The field test and numerical analysis results of calcareous sand as shown in Fig. 18. An empirical prediction formula for the crater diameter as a function of the TNT equivalence and the burial depth of the explosives has been proposed, as shown in Eq. (4):

$$\ln(D/d) = 0.731 + 0.623 \ln(1/z - 0.767) \quad (4)$$

where, z is the scaled burial depth of the explosive, D is the diameter of the crater, and d is the burial depth of the explosive.

Discussion

In this study, the types and sizes of craters in calcareous sand foundations were examined using field tests and the SPH-FEM coupling algorithm. The results obtained from the SPH-FEM coupling algorithm were largely consistent with the field test outcomes, demonstrating that the SPH-FEM coupling algorithm can effectively avoid non-convergence issues due to element distortion when addressing large deformation problems caused by explosions in sand.

Based on the results of field tests and numerical simulations, it is evident that the scaled burial depth of explosives plays a decisive role in determining the type and size of the explosion crater. There are three types of explosion craters with different scaled burial depths, when the scaled burial depth is less than $1.11 \text{ m/kg}^{1/3}$, the crater is ejecta-type; when the scaled burial depth is in the range of $1.11 \sim 2.05 \text{ m/kg}^{1/3}$, the crater is collapse-type crater; when the scaled burial depth is greater than $2.05 \text{ m/kg}^{1/3}$, a camouflet explosion phenomenon occurred.

In the ejecta-type explosion crater, the size of the explosion crater first increases and then decreases as the burial depth of the explosive increases. When the scaled burial depth is $0.53 \text{ m/kg}^{1/3}$, the diameter of the explosion crater reaches the maximum. The main reason is that when the scaled burial depth is less than $0.53 \text{ m/kg}^{1/3}$, the energy generated by the explosion is more dissipated through the ground surface. As the scaled burial depth increases, the energy generated by the explosion acts more in sand. When the scaled burial depth is greater than $0.53 \text{ m/kg}^{1/3}$, the inhibitory effect of the sand above the explosive on the explosion gradually increases, and the size of the explosion crater gradually decreases, and even changes the type of explosion crater from the ejecta-type to the collapse-type.

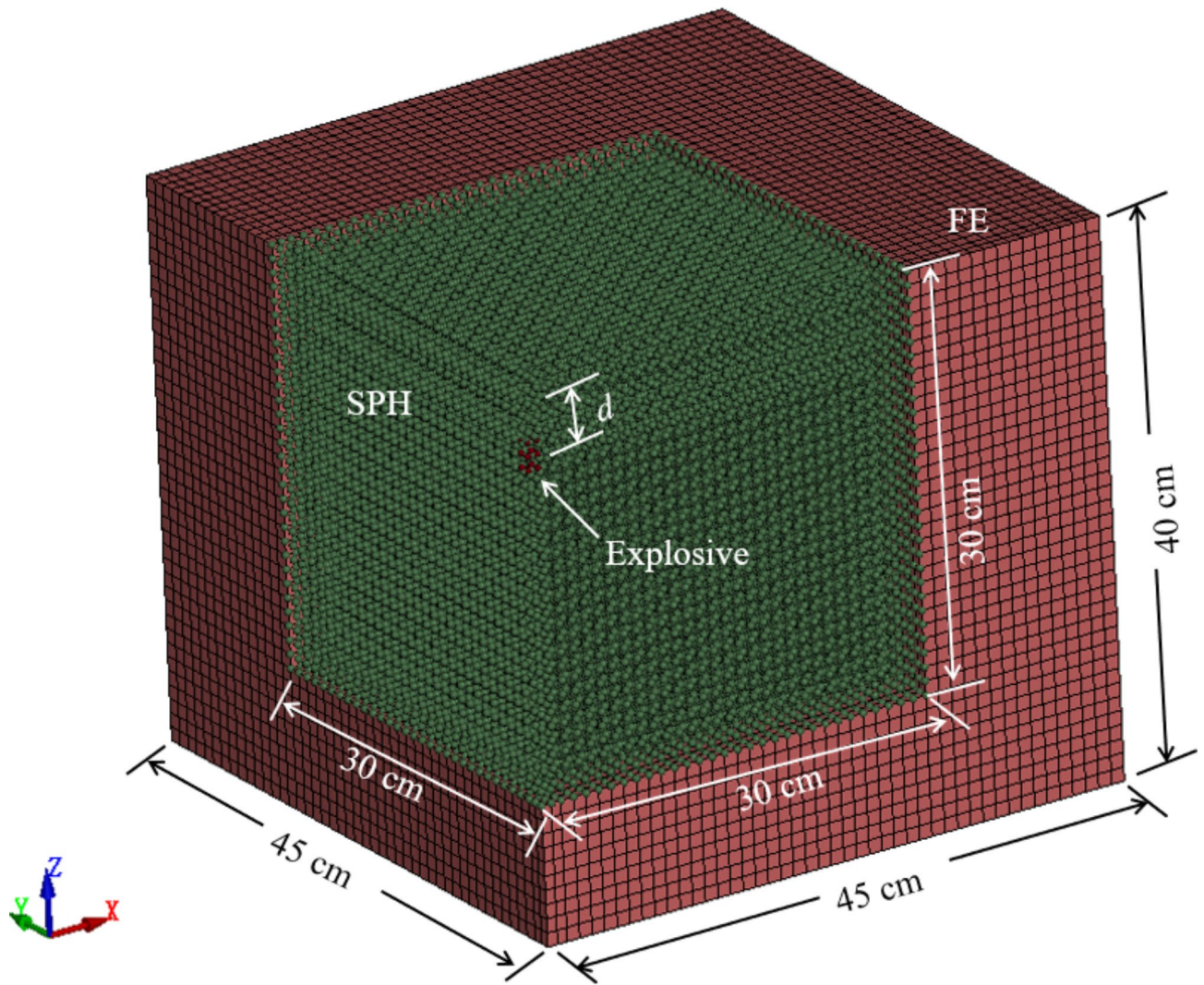


Fig. 9. 3D SPH-FEM model of a quarter.

The results of calcareous sand and other's results as shown in Fig. 19. The explosion crater in calcareous sand is similar to results observed in other's researches^{10,13,19,33}. However, the size of the explosion crater in the calcareous sand foundation is quite different. The size of the crater in the calcareous sand foundation is larger than 40% than other's results while the scaled of burial depth is same. The primary reason is that calcareous sand particles have more surface pores and a lower specific gravity compared to quartz sand.

This study mainly studies the influence of scaled burial depth on the type and size of crater, based on field tests or numerical simulations. However, in fact, when the calcareous sand particles are subjected to high-frequency loading during the explosion, inevitable particle fragmentation will occur. The fragmentation of calcareous sand particles is mainly concentrated in a small number of particles near the explosive, which can be ignored when studying the type and size of explosion craters. This study focus on the type and size of crater in calcareous sand foundations through field tests and SPH-FEM coupling algorithm still has important reference value.

Conclusions

In this paper, we studied the crater's type and size of calcareous sand foundation, and found that the SPH-FEM algorithm can better reflect the formation process of explosion craters and the movement trajectories of particles. We obtained the critical scaled burial depth for different type of crater, and derived an empirical prediction formula for calcareous sand. The results provide a theoretical basis for anti-explosion design in calcareous sand foundations.

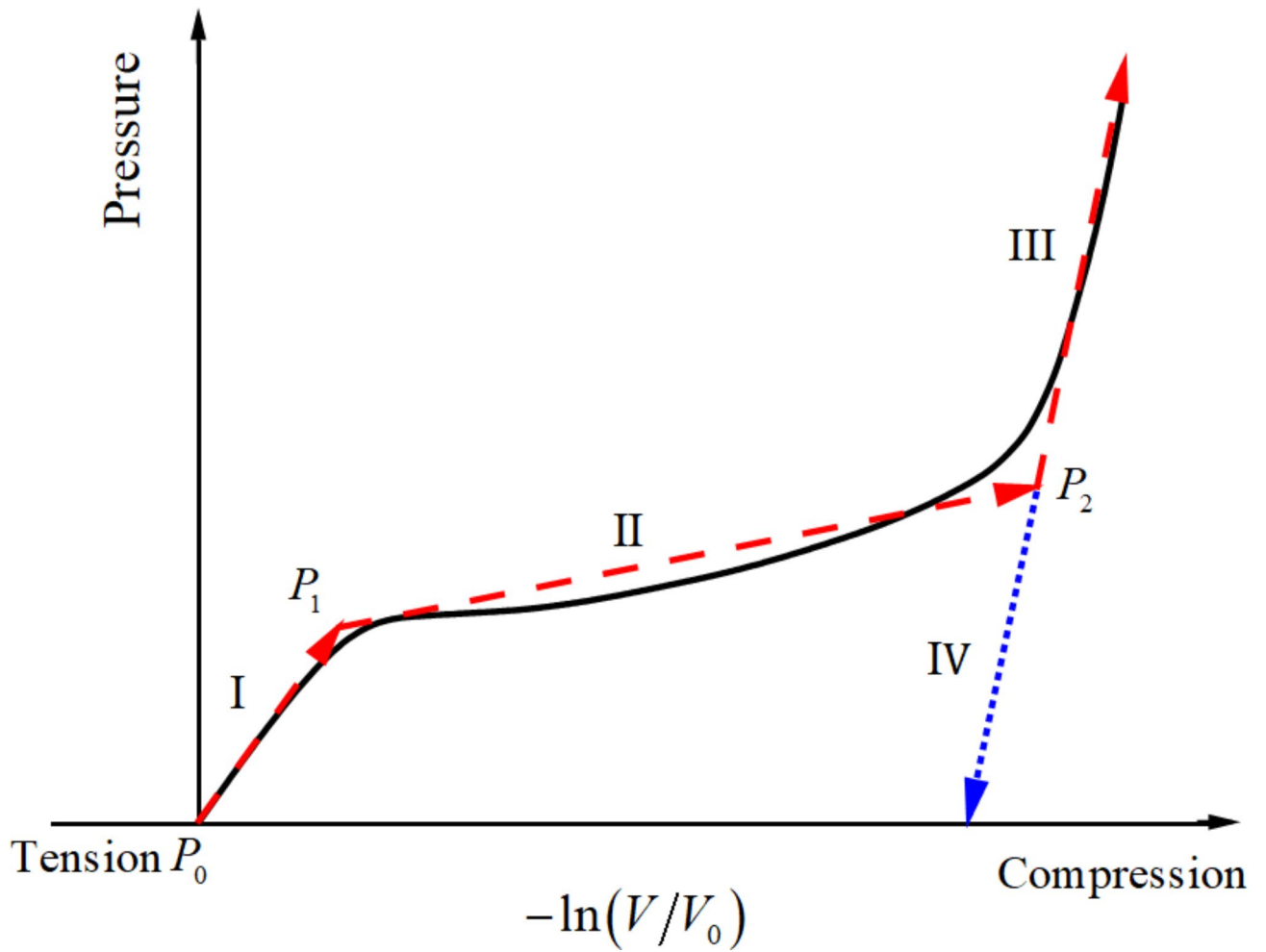


Fig. 10. Schematic of pressure versus volume response for sand.

No.	$\ln(V/V_0)$	P/MPa	No.	$\ln(V/V_0)$	P/MPa
1	0.00	0	6	0.25	15.83
2	0.02	2.3	7	0.30	21.03
3	0.10	5.8	8	0.40	36.43
4	0.15	8.5	9	0.50	62.23
5	0.20	11.7	10	0.60	105.09

Table 3. Parameters of state equation of calcareous sand.

$\rho(kg/m^3)$	$v_D(m/s)$	$P_{Cj}(GPa)$	$A/(GPa)$	$B/(GPa)$	R_1	R_2	ω	$E_0(GPa)$
1630	6930	21	373.8	3.747	4.15	0.9	0.35	4.0

Table 4. Material parameters of explosive model.

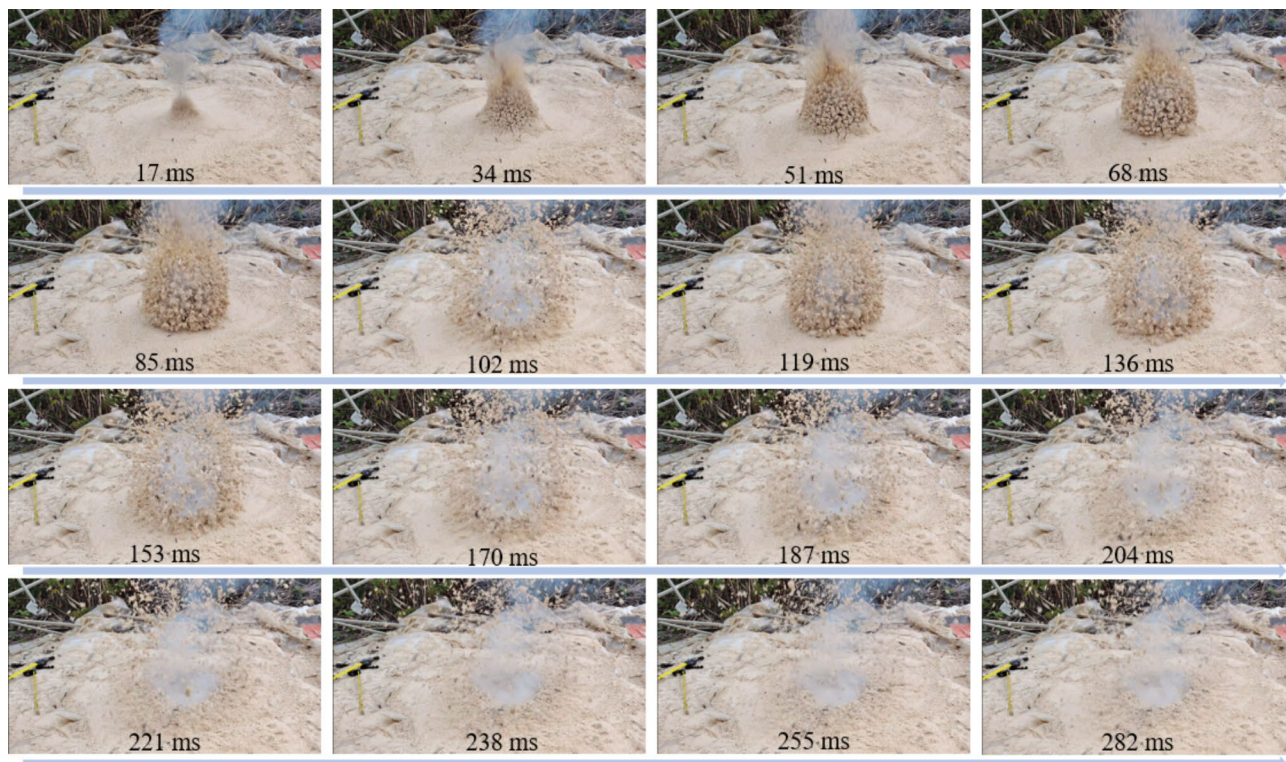


Fig. 11. The formation process of the crater (Condition BE2).

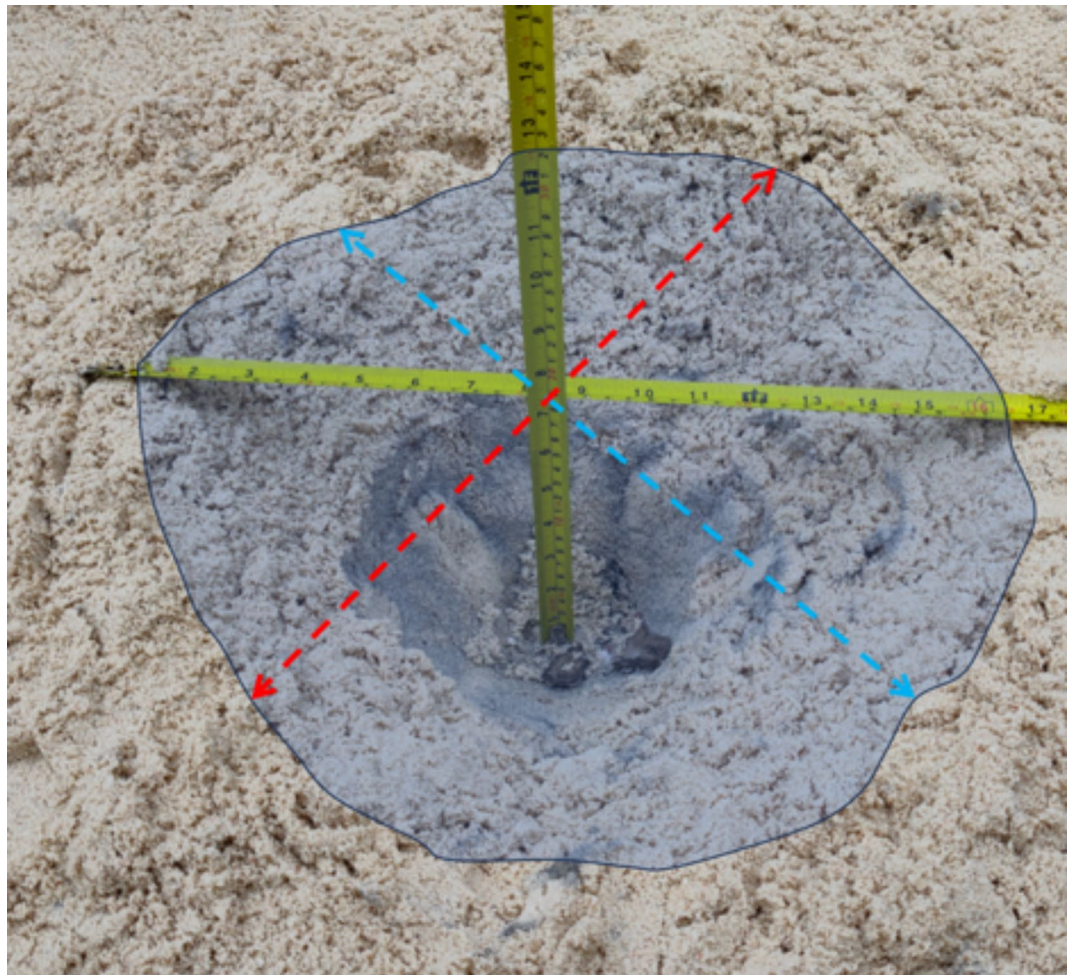


Fig. 12. Diameter of crater (Condition BE4).

Test	The scaled depth (m/ kg ^{1/3})	Crater dimensions/ (m)		Test	The scaled depth (m/ kg ^{1/3})	Crater dimensions/(m)	
		D	d			D	d
BE1	0.18	0.32	0.10	BE5	0.64	0.41	0.22
		0.35	0.13			0.38	0.22
		0.34	0.11			0.37	0.23
BE2	0.29	0.36	0.13	BE6	0.76	0.38	0.22
		0.37	0.15			0.35	0.25
		0.35	0.12			0.36	0.23
BE3	0.41	0.39	0.17	BE7	0.88	0.31	0.25
		0.43	0.17			0.35	0.26
		0.41	0.16			0.33	0.24
BE4	0.53	0.44	0.19	BE8	0.99	0.30	0.27
		0.42	0.19			0.33	0.28
		0.45	0.21			0.31	0.28

Table 5. Results of crater size under different scaled burial depth.

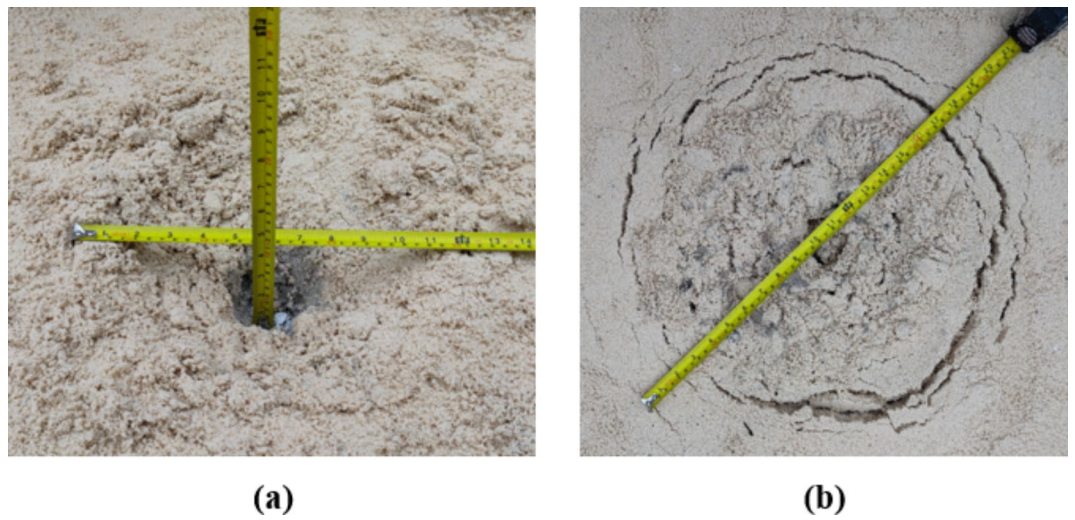


Fig. 13. The type of the crater. (a) Ejecta-type crater (Condition BE2). (b) Collapse-type crater (Condition BE9).

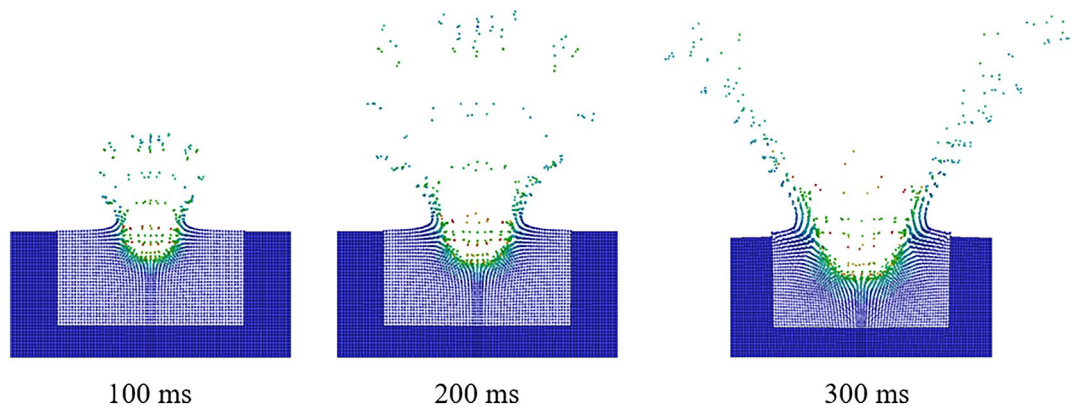


Fig. 14. The formation process of the ejecta-type crater.

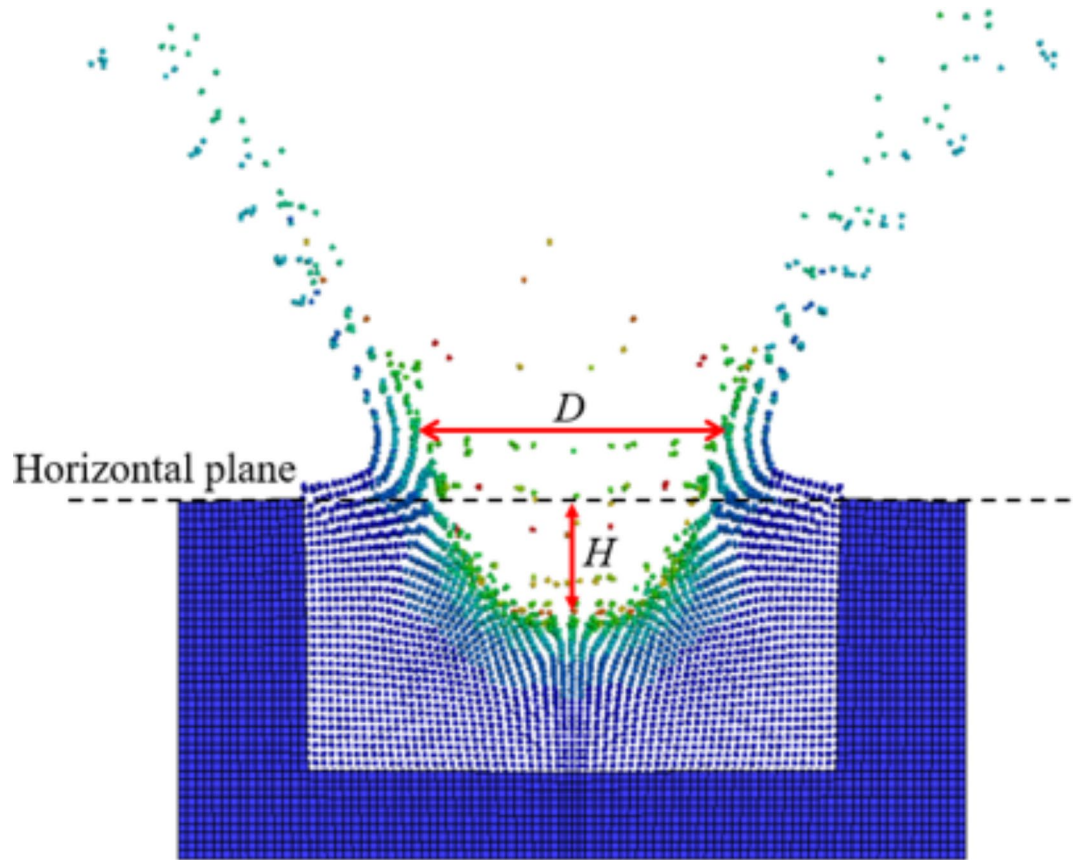


Fig. 15. Diameter and depth of crater.

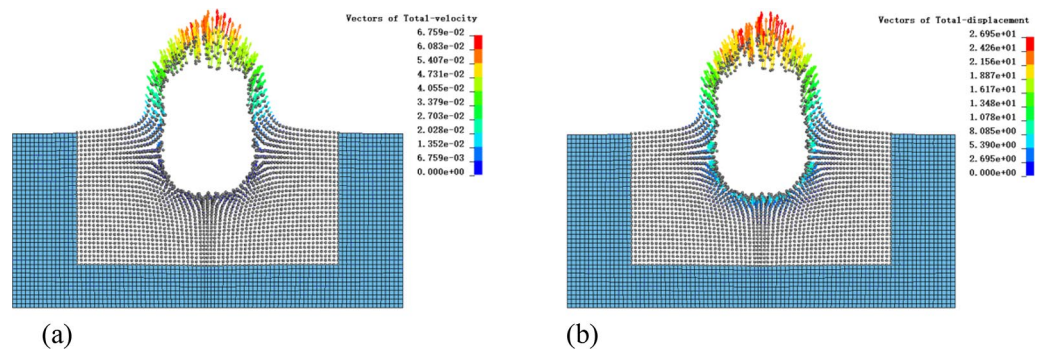


Fig. 16. Vector field of the velocity and displacement. (a) Vector field of velocity. (b) Vector field of displacement

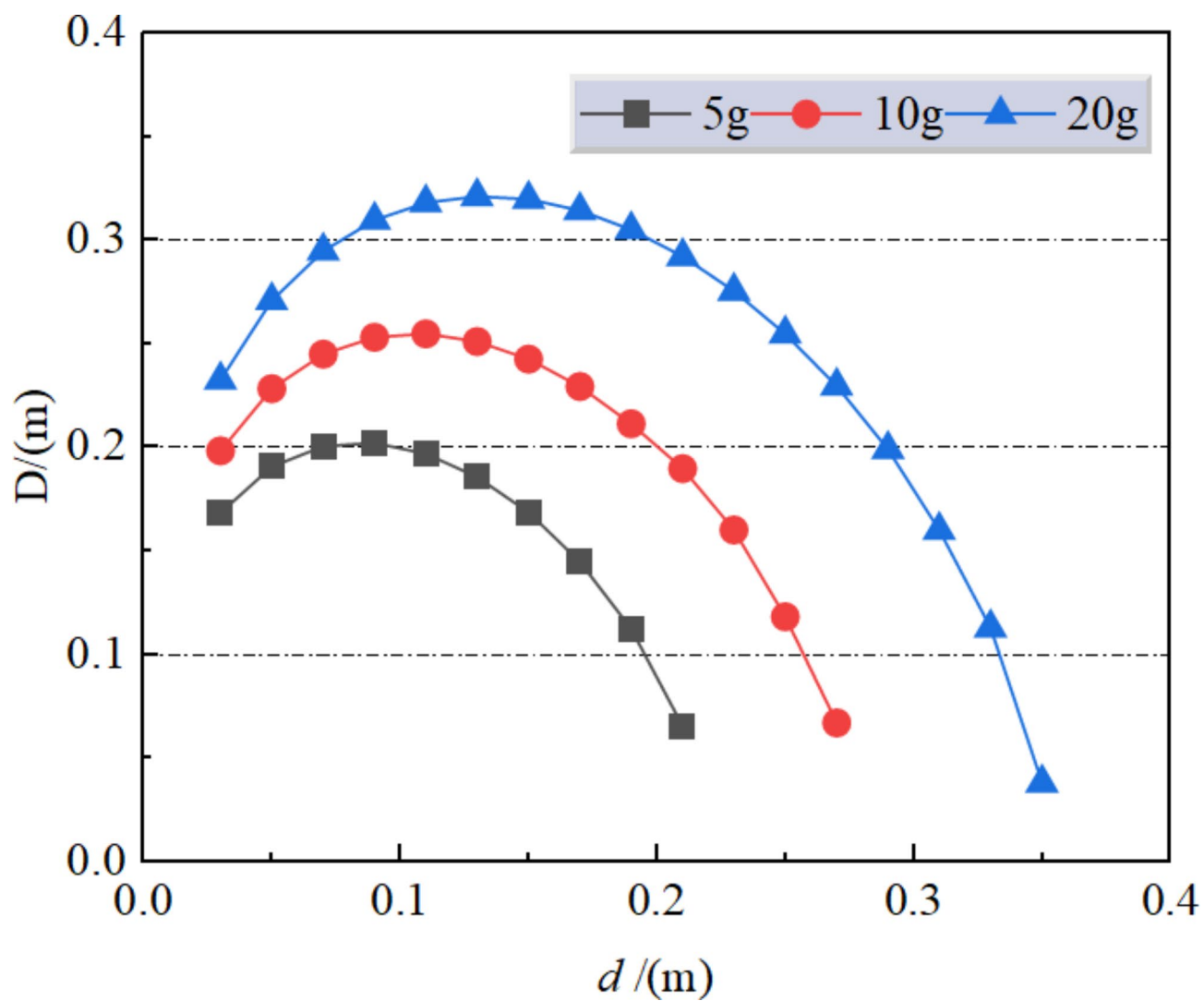


Fig. 17. Diameter of the crater under different TNT equivalents.

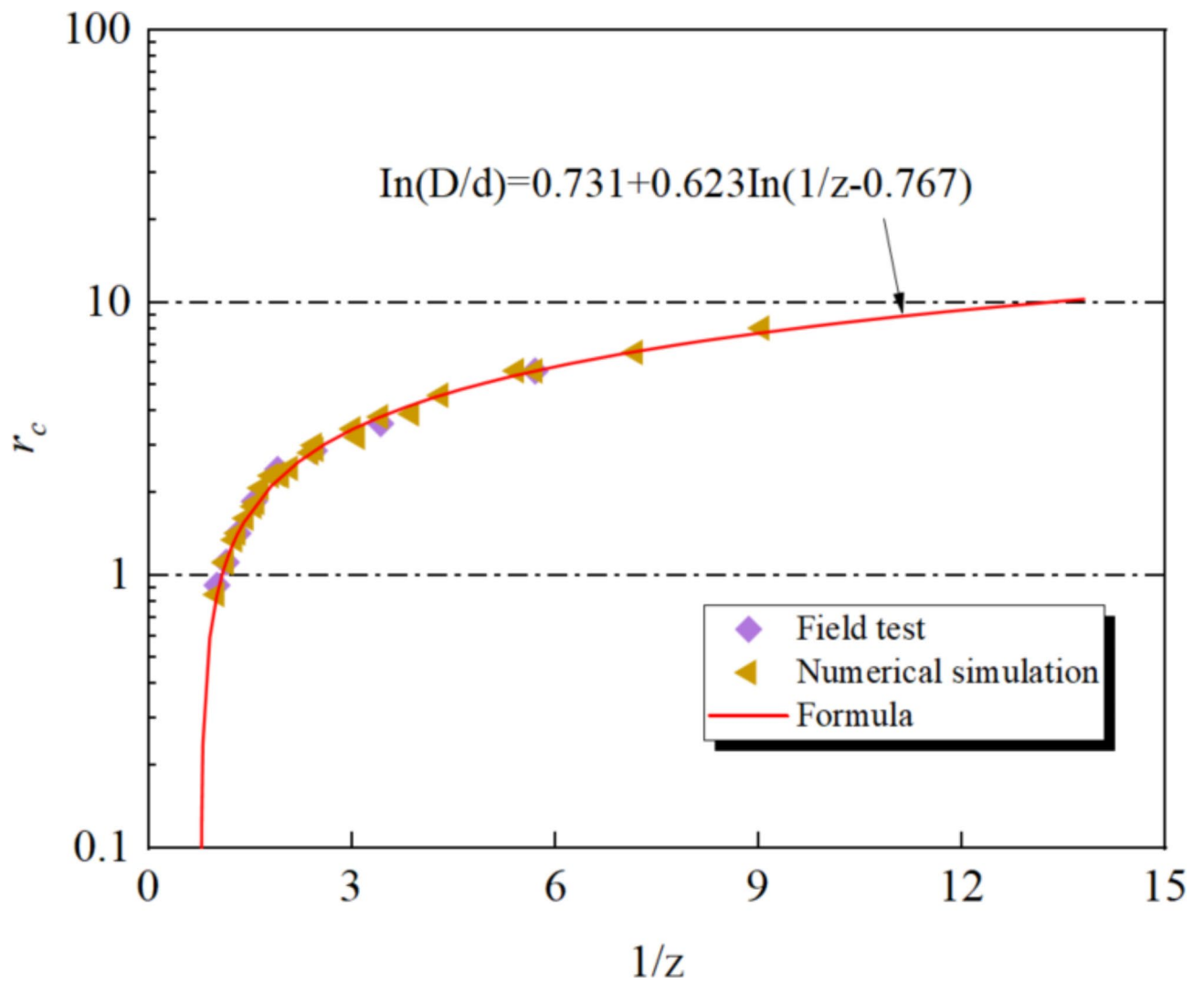


Fig. 18. Relationship between diameter of crater and scaled burial depth.

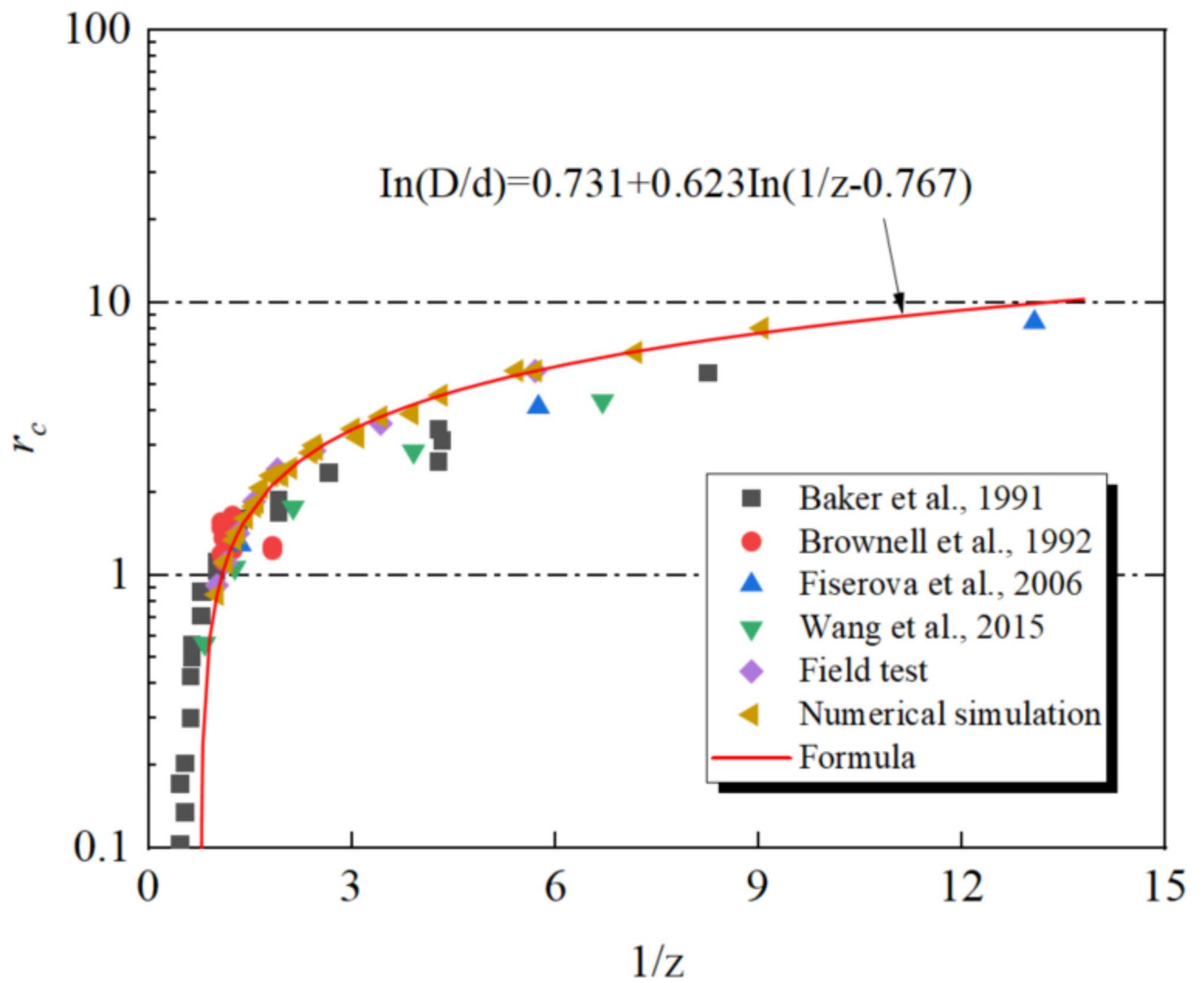


Fig. 19. Relationship between diameter of crater and scaled burial depth compared other's results.

Data availability

The datasets used and/or analyzed during the current study available from the corresponding author on reasonable request.

Received: 10 August 2024; Accepted: 8 October 2024

Published online: 27 October 2024

References

- Zhang, Z., Chen, Y., Liu, H., Zhou, Y. & Zhou, X. Resistivity characteristics during horizontal-layered electrolysis desaturation of calcareous sand. *Eng Geol* **279**, 105899. <https://doi.org/10.1016/j.enggeo.2020.105899> (2020).
- Gao, H. et al. Flowability of Saturated Sands under Cyclic Loading and the Viscous Fluid Flow failure Criterion for Liquefaction triggering. *J Geotech Geoenvironmental Eng* **150**, 1–15. <https://doi.org/10.1061/jggefkg.teng-11872> (2024).
- Peng, Y., Ding, X., Xiao, Y., Deng, X. & Deng, W. Detailed amount of particle breakage in nonuniformly graded sands under one-dimensional compression. *Can Geotech J* **57**, 1239–46. <https://doi.org/10.1139/cgj-2019-0283> (2020).
- Peng, Y., Ding, X., Xiao, Y., Deng, X. & Deng, W. Detailed amount of particle breakage in multi-sized coral sands under impact loading. *Eur J Environ Civ Eng* **26**, 2344–53. <https://doi.org/10.1080/19648189.2020.1762750> (2022).
- Ding X, Zhang Y, Wu Q, Chen Z, Wang C. Shaking table tests on the seismic responses of underground structures in coral sand. *Tunn Undergr Sp Technol* **2021**;109. <https://doi.org/10.1016/j.tust.2020.103775>.
- Hailiang, W. & Chaoliang, Y. Change rules of physical and mechanical properties of soil after explosion into cavity. *Rock Soil Mech* **7598**, 2617–22. <https://doi.org/10.16285/j.rsm.2011.09.014> (2011).
- Wang, W., Chen, Y., Liu, H. & Zhou, F. Experimental investigation of dynamic porewater pressure response induced by single shallow-buried detonations in saturated sand. *Geotech Lett* **5**, 142–6. <https://doi.org/10.1680/jgele.14.00083> (2015).
- Wang, M., Qiu, Y. & Yue, S. Similitude laws and modeling experiments of explosion cratering in multi-layered geotechnical media. *Int J Impact Eng* **117**, 32–47. <https://doi.org/10.1016/j.ijimpeng.2017.11.018> (2018).
- Wang Weiguo, Fang & Jizhi, Gu Jungang, C. Y. MM-ALE simulation of strip explosive charge breaking embankment. *J Disaster Prev Mitig Eng* **38**, 87–92 (2018).
- Baker, W. E. *Similarity Methods in Engineering Dynamics: Theory and Practice of Scale Modeling* (Elsevier, Amsterdam, 1991).
- Livingston CW. Scaled charge depth. Google Patents 1974.
- Pokrovskii GI. Blasting. Moscow: Nedra. Nedra 1973.
- Boreskov, M. M. Experience in Mining Engineering. St Petersburg Dep Princ Press 1869:7–18.
- Ashford, S. A., Rollins, K. M. & Lane, J. D. Blast-Induced Liquefaction for full-Scale Foundation Testing. *J Geotech Geoenvironmental Eng* **130**, 798–806. [https://doi.org/10.1061/\(asce\)1090-0241](https://doi.org/10.1061/(asce)1090-0241) (2004).
- Ambrosini, R. D., Luccioni, B. M., Danesi, R. F., Riera, J. D. & Rocha, M. M. Size of craters produced by explosive charges on or above the ground surface. *Shock Waves* **12**, 69–78. <https://doi.org/10.1007/s00193-002-0136-3> (2002).
- Yongsheng, J. & Wangweiguo, Xianqi, X. Experiment on the characteristics of explosion pit formation in sandy soil with low moisture content and saturated sands. *Explos Shock Waves* **37**, 799–806 (2017).
- Wang, W., Chen, Y., Yang, G. & Liu, Y. Field tests and numerical simulations of blast-induced crater in wet sands. *Yanshilixue Yu Gongcheng Xuebao/Chinese J Rock Mech* **35**, 68–75. <https://doi.org/10.13722/j.cnki.jrme.2015.0171> (2016).
- Wang, Z., Lu, Y. & Bai, C. Numerical analysis of blast-induced liquefaction of soil. *Comput Geotech* **35**, 196–209. <https://doi.org/10.1016/j.compgeo.2007.04.006> (2008).
- Wang Weiguo, Chen & Yumin, Liu Hanlong, Z. Z. Numerical study on soil explosion effect based on SPH-FEM coupling method. *Rock Soil Mech* **34**, 2014–22. <https://doi.org/10.16285/j.rsm.2013.07.015> (2013).
- Xiao, N., Zhou, X. P. & Gong, Q. M. The modelling of rock breakage process by TBM rolling cutters using 3D FEM-SPH coupled method. *Tunn Undergr Sp Technol* **61**, 90–103. <https://doi.org/10.1016/j.tust.2016.10.004> (2017).
- Hu, Y., Lu, W., Chen, M., Yan, P. & Zhang, Y. Numerical simulation of the complete rock blasting response by SPH-DAM-FEM approach. *Simul Model Pract Theory* **56**, 55–68. <https://doi.org/10.1016/j.simpat.2015.04.001> (2015).
- Wang Z, Zheng D, Guo X, Gu Z, Shen Y, Nian T. Investigation of offshore landslides impact on bucket foundations using a coupled SPH-FEM method. *Geoenvironmental Disasters* **2024**;11. <https://doi.org/10.1186/s40677-024-00266-9>.
- Jimenez Fernandez, J. C. et al. 3D numerical simulation of slope-flexible system interaction using a mixed FEM-SPH model. *Ain Shams Eng J* **13**, 101592. <https://doi.org/10.1016/j.asej.2021.09.019> (2022).
- Wang, W., Wu, Y., Wu, H., Yang, C. & Feng, Q. Numerical analysis of dynamic compaction using FEM-SPH coupling method. *Soil Dyn Earthq Eng* **140**, 106420. <https://doi.org/10.1016/j.soildyn.2020.106420> (2021).
- Jayasinghe, L. B., Waldmann, D. & Shang, J. Impact of Pile punching on adjacent piles: insights from a 3D coupled SPH-FEM analysis. *Appl Mech* **1**, 47–58. <https://doi.org/10.3390/applmech1010004> (2020).
- Liang, S. & Chen, Z. SPH-FEM coupled simulation of SSI for conducting seismic analysis on a rectangular underground structure. *Bull Earthq Eng* **17**, 159–80. <https://doi.org/10.1007/s10518-018-0456-z> (2019).
- Qi B, Yang F, He H. Research on Dynamic Response of Buried Pipeline Under Explosion Load Based on SPH-FEM Method. vol. 510 LNCE. Springer Nature Switzerland; 2024. https://doi.org/10.1007/978-3-031-60765-3_19.
- Koneshwaran, S., Thambiratnam, D. P. & Gallage, C. Response of segmented bored transit tunnels to surface blast. *Adv Eng Softw* **89**, 77–89. <https://doi.org/10.1016/j.advengsoft.2015.02.007> (2015).
- De, A. Numerical simulation of surface explosions over dry, cohesionless soil. *Comput Geotech* **43**, 72–9. <https://doi.org/10.1016/j.compgeo.2012.02.007> (2012).
- Lu, Y., Wang, Z. & Chong, K. A comparative study of buried structure in soil subjected to blast load using 2D and 3D numerical simulations. *Soil Dyn Earthq Eng* **25**, 275–88. <https://doi.org/10.1016/j.soildyn.2005.02.007> (2005).
- Huang, X., Yue, Y., Zhu, B. & Chen, Y. Failure analysis of underground concrete silo under near-field soil explosion. *Tunn Undergr Sp Technol* **147**, 105696. <https://doi.org/10.1016/j.tust.2024.105696> (2024).
- Luccioni, B., Ambrosini, D., Nurick, G. & Snyman, I. Craters produced by underground explosions. *Comput Struct* **87**, 1366–73. <https://doi.org/10.1016/j.compstruc.2009.06.002> (2009).
- FIŠEROVÁ D. Numerical Analyses of Buried Mine Explosions With Emphasis on Effect of Soil Properties on Loading. 2006.
- Mandal, J., Goel, M. D. & Agarwal, A. K. Surface and buried explosions: an explorative review with recent advances. *Arch Comput Methods Eng* **28**, 4815–35. <https://doi.org/10.1007/s11831-021-09553-2> (2021).
- ZM Z, BM. X. A Suggestion on Theoretical Calculation of Underground Nuclear Explosion. 2nd Ed Zheng Zhemin Collect 2004.
- Clarke, S. D., Rigby, S. E., Fay, S. D., Tyas, A., Reay, J. J., Warren, J. A., et al. “Bubble-type” vs “shock-type” Loading from Buried Explosives. In *16th Int Symp Interact Eff Munitions with Struct* 2015.
- Esmaili, M. & Tavakoli, B. Finite element method simulation of explosive compaction in saturated loose sandy soils. *Soil Dyn Earthq Eng* **116**, 446–59. <https://doi.org/10.1016/j.soildyn.2018.09.048> (2019).
- Holsapple, K. A. & Schmidt, R. M. On the scaling of crater dimensions – 2. Impact processes. *J Geophys Res* **87**, 1849–70. <https://doi.org/10.1029/JB087iB03p01849> (1982).
- Luccioni, B. & Ambrosini, D. Effect of buried explosions. *Mecánica Comput* **26**, 2656–73 (2007).

40. Zhou, H. et al. Centrifuge and numerical modelling of the seismic response of tunnels in two-layered soils. *Tunn Undergr Sp Technol* **113**, 103980. <https://doi.org/10.1016/j.tust.2021.103980> (2021).
41. Zhang, Q., Xiang, C. & Liang, H. M. Prediction of the explosion effect of aluminized explosives. *Sci China Physics, Mech Astron* **56**, 1004–9. <https://doi.org/10.1007/s11433-013-5054-0> (2013).
42. Pan, Y., Li, J., Zong, Z., Wu, C. & Qian, H. Experimental and numerical study on ground shock propagation in calcareous sand. *Int J Impact Eng* **180**, 1–13. <https://doi.org/10.1016/j.ijimpeng.2023.104724> (2023).
43. Sigalotti, L. D. G., Klapp, J. & Gesteira, M. G. The mathematics of smoothed particle hydrodynamics (SPH) consistency. *Front Appl Math Stat* **7**, 1–16. <https://doi.org/10.3389/fams.2021.797455> (2021).
44. Park, H. J. & Seo, H. D. A new SPH-FEM coupling method for fluid–structure interaction using segment-based interface treatment. *Eng Comput* **40**, 1127–43. <https://doi.org/10.1007/s00366-023-01856-1> (2023).
45. Zhang Zhichun, Qiang Hongfu, G. W. A new SPH-FEM coupling algorithm and its application in impact dynamics problems. *Explos Shock Waves* **31**, 243–50 (2011).
46. Ng, K. C., Ng, Y. L., Sheu, T. W. H. & Alexiadis, A. Assessment of Smoothed Particle Hydrodynamics (SPH) models for predicting wall heat transfer rate at complex boundary. *Eng Anal Bound Elem* **111**, 195–205. <https://doi.org/10.1016/j.enganabound.2019.10.017> (2020).
47. Yang, Y., Xie, X. & Wang, R. Numerical simulation of dynamic response of operating Metro tunnel induced by ground explosion. *J Rock Mech Geotech Eng* **2**, 373–84. <https://doi.org/10.3724/SPJ.1235.2010.00373> (2010).
48. Zhichao, Z., Yumin, C., Hanlong, L. & Weiguo, W. Analysis of the influence of pore water pressure and explosive burial depth on the explosion effect of dams Zhang Zhichao. *Rock Soil Mech* **33**, 2214–20. <https://doi.org/10.16285/j.rsm.2012.07.033> (2012).
49. Wu, T., Zong, Z., Li, M., Gan, L. & Wu, J. Numerical simulation of basic liquefaction of saturated calcareous sand under the action of shallowly buried single charge pack explosion. *J Southeast Univ* **52**, 237–46 (2022).
50. Chen, Y. et al. Study on the liquefaction characteristics of saturated sands by millisecond delay blasting. *Soil Dyn Earthq Eng* **164**, 107584. <https://doi.org/10.1016/j.soildyn.2022.107584> (2023).

Acknowledgements

This work was supported by the National Natural Science Foundation of China (Grant nos. 52179101) and Key Laboratory of Blasting Engineering in Hubei Province (Grant nos. 523007912).

Author contributions

Changchun Li: Conduct field tests, numerical simulations and wrote the main manuscript. Yumin Chen: Provide guidance for numerical analysis, field tests and paper writing. Yingkang Yao: Provide guidance for field tests. Yonggang Gou: Provide guidance for numerical analysis. Qiongtong Wang: Conducting field test and numerical analysis. Junwei Guo: Conducting field test. Xiao Xie: Conducting numerical analysis. Xiangyu Wang: Revision of the English version of the main manuscript.

Declarations

Competing interests

The authors declare no competing interests.

Additional information

Correspondence and requests for materials should be addressed to Y.C. or X.W.

Reprints and permissions information is available at www.nature.com/reprints.

Publisher's note Springer Nature remains neutral with regard to jurisdictional claims in published maps and institutional affiliations.

Open Access This article is licensed under a Creative Commons Attribution-NonCommercial-NoDerivatives 4.0 International License, which permits any non-commercial use, sharing, distribution and reproduction in any medium or format, as long as you give appropriate credit to the original author(s) and the source, provide a link to the Creative Commons licence, and indicate if you modified the licensed material. You do not have permission under this licence to share adapted material derived from this article or parts of it. The images or other third party material in this article are included in the article's Creative Commons licence, unless indicated otherwise in a credit line to the material. If material is not included in the article's Creative Commons licence and your intended use is not permitted by statutory regulation or exceeds the permitted use, you will need to obtain permission directly from the copyright holder. To view a copy of this licence, visit <http://creativecommons.org/licenses/by-nc-nd/4.0/>.

© The Author(s) 2024